

# JGR Solid Earth

## RESEARCH ARTICLE

10.1029/2022JB024344

### Key Points:

- We develop a method to estimate meter-scale elevation changes from SAR amplitude observations and validate it against independent analyses
- Applied to the 2019–2020 Shishaldin volcanic eruption, this quantifies elevation changes that correlate with observed volcanic activity
- We quantify unresolved cone growth at Shishaldin Volcano in November 2019, collapse events in spring 2020, and lava flow activity

### Supporting Information:

Supporting Information may be found in the online version of this article.

### Correspondence to:

M. Angarita,  
[mfangaritasr@alaska.edu](mailto:mfangaritasr@alaska.edu)






### Citation:

Angarita, M., Grapenthin, R., Plank, S., Meyer, F. J., & Dietterich, H. (2022). Quantifying large-scale surface change using SAR amplitude images: Crater morphology changes during the 2019–2020 Shishaldin volcano eruption. *Journal of Geophysical Research: Solid Earth*, 127, e2022JB024344. <https://doi.org/10.1029/2022JB024344>

Received 7 MAR 2022

Accepted 10 AUG 2022

## Quantifying Large-Scale Surface Change Using SAR Amplitude Images: Crater Morphology Changes During the 2019–2020 Shishaldin Volcano Eruption

M. Angarita<sup>1</sup> , R. Grapenthin<sup>1</sup> , S. Plank<sup>2</sup> , F. J. Meyer<sup>1</sup> , and H. Dietterich<sup>3</sup> 

<sup>1</sup>Geophysical Institute and Department of Geosciences, University of Alaska Fairbanks, Fairbanks, AK, USA, <sup>2</sup>German Aerospace Center (DLR), German Remote Sensing Data Center, Oberpfaffenhofen, Germany, <sup>3</sup>U.S. Geological Survey, Alaska Volcano Observatory, Anchorage, AK, USA

**Abstract** Morphological processes often induce meter-scale elevation changes. When a volcano erupts, tracking such processes provides insights into the style and evolution of eruptive activity and related hazards. Compared to optical remote-sensing products, synthetic aperture radar (SAR) observes surface change during inclement weather and at night. Differential SAR interferometry estimates phase change between SAR acquisitions and is commonly applied to quantify deformation. However, large deformation or other coherence loss can limit its use. We develop a new approach applicable when repeated digital elevation models (DEMs) cannot be otherwise retrieved. Assuming an isotropic radar cross-section, we estimate meter-scale vertical morphological change directly from SAR amplitude images via an optimization method that utilizes a high-quality DEM. We verify our implementation through simulation of a collapse feature that we modulate onto topography. We simulate radar effects and recover the simulated collapse. To validate our method, we estimate elevation changes from TerraSAR-X stripmap images for the 2011–2012 eruption of Mount Cleveland. Our results reproduce those from two previous studies; one that used the same dataset, and another based on thermal satellite data. By applying this method to the 2019–2020 eruption of Shishaldin Volcano, Alaska, we generate elevation change time series from dozens of co-registered TerraSAR-X high-resolution spotlight images. Our results quantify previously unresolved cone growth in November 2019, collapses associated with explosions in December–January, and further changes in crater elevations into spring 2020. This method can be used to track meter-scale morphology changes for ongoing eruptions with low latency as SAR imagery becomes available.

**Plain Language Summary** Rapidly occurring geologic processes, such as volcanic eruptions or landslides, can cause drastic, meter-scale changes in local surface elevation. Optical images often used to calculate these changes cannot be relied on under poor acquisition conditions such as inclement weather or nighttime. However, several satellite missions record radar signals reflected from Earth's surface, which are less affected by cloudy views or darkness. We develop a new method to estimate elevation changes directly from the strength of such reflected radar signals. To reference the results appropriately, we require a digital elevation model (DEM) with a known acquisition time such that it can be related to the process under investigation. We verify our software by simulating a crater collapse and recovering it from the data. We validate our method against independent observations of elevation changes at Mount Cleveland, Alaska, in 2011–2012. Lastly, we estimate surface elevation changes during the 2019–2020 eruption at Shishaldin Volcano, Alaska, for which the TerraSAR-X satellite mission acquired several radar images. We resolve increases in elevation in the first stages of the eruption and collapses associated with explosions in spring 2020, and changes due to lava flow activity. The method resolves processes to an accuracy of about 1–3 m.

## 1. Introduction

Short-term geological processes, such as landslides, volcanic eruptions, or sinkhole formation, produce rapid and significant topographic change often exceeding tens of meters. Geodetic data can be used to gain insight into these processes. For instance, to understand and assess landslides, we require an estimate of onset and duration of creep before failure (e.g., Intrieri et al., 2019; Saito, 1969), in addition to the influence of other types of geological and meteorological processes (earthquakes and/or rainfall). Surface deformation observations due to volcanic activity can provide possible volume changes and first order geometries for magma storage and migra-

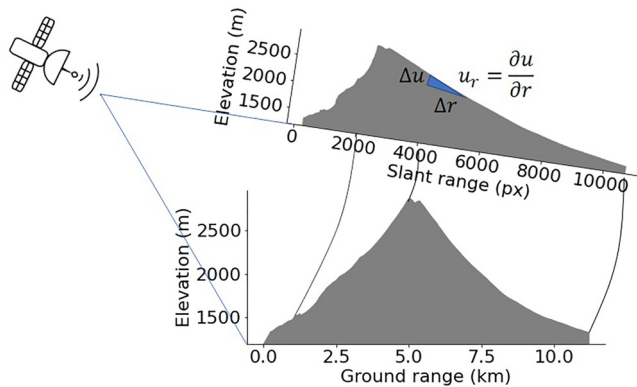


**Figure 1.** Projection of a digital elevation model into the line-of-sight observation geometry of the satellite, highlighting the gradient of the topography with respect to slant range.

tion (e.g., Poland et al., 2006). However, to detect and analyze very shallow processes at or near the surface, we require observations close enough to the signal source to resolve a signal above the noise floor. While interferometric synthetic aperture radar (InSAR) analysis can quantify low-rate deformation using radar signal phase data (e.g., Pritchard & Simons, 2002), large surface disturbances associated with eruption or mass-wasting processes often result in loss of phase coherence induced by phase aliasing in the case of resurfacing by eruptive deposits and thus decorrelation in regions of most interest (e.g., Massonnet et al., 1993). Nevertheless, InSAR techniques can be used to calculate elevation maps when the SAR acquisitions are taken from substantially different orbital positions and the time span between observations is negligible (e.g., Zebker et al., 1994; Zhang et al., 2021).

To resolve such topographic change from SAR, past applications at volcanoes have relied on large numbers of SAR acquisitions. For instance, Ebmeier et al. (2012) were able to retrieve large scale topography changes from a comparison of post-event SAR phase data with a pre-event DEM, but their method requires several SAR acquisitions to succeed. Similarly, several studies have used bistatic satellite missions like TanDEM-X (Zink

et al., 2014) to retrieve elevation changes calculating multiple DEMs achieving an uncertainty of 4 m. These types of missions require two satellites: one that emits the radar signal and receives the reflected signal, while the other passively receives the reflected signal, resulting in two SAR images. The phase information from both can be used to calculate interferograms in which phase change represents an estimate of topography. The resulting DEM can be restimated at the period at which a satellite revisits the same ground location (Kubaneck et al., 2021). Poland (2014) used this technique with TanDEM-X data to quantify lava discharge rates at Kilauea Volcano, Hawai'i. Similarly, Kubaneck, Richardson, et al. (2015) used TanDEM-X and Shuttle Radar Topography Mission (SRTM) data to quantify lava flow volumes at Tolbachik volcano, Kamchatka, during its 2012–2013 eruption. They also applied TanDEM-X data to estimate lava dome volume changes at Merapi during its 2010 eruption (Kubaneck, Westerhaus, et al., 2015). However, most SAR missions consist of just one satellite and although there have been efforts to calculate DEMs from short temporal baseline re-acquisitions (Lombardi et al., 2016), the loss of coherence in highly vegetated areas or places with snow cover reduces the accuracy of the retrieved DEMs.

The amplitude data of SAR images, on the other hand, offer an underutilized avenue to quantify topography and topographic change. Pallister et al. (2013) and Wang et al. (2015) developed methods to track lava dome volume variations at Merapi and Mount Cleveland volcanoes, respectively. Both methods project geometric features of the summit into radar coordinates to simulate the growth of a dome and then compare these simulations with the amplitude images to estimate elevation change. This presents a drawback as these approaches require knowledge of the physical process, availability of a model, and well-constrained parameters to reproduce the process, which makes them perhaps best applicable to slow, long-term processes.

It is possible, however, to estimate topographic information directly from the shading in optical or radar images without requiring a model of the process because shading provides information about the shape of the illuminated target. If we know the surface reflectivity function and the position of the illumination source (Horn, 1975; Toutin & Gray, 2000), we can estimate surface slope and elevation; this is known as photoclinometry. Radioclinometry is an adaptation of photoclinometry to radar images that was developed by Wildey (1984) and has been successfully applied to the retrieval of topographic features from radar amplitude images (Frankot & Chellappa, 1990; Thomas et al., 1991; Wildey, 1984). Oblique imaging effects such as foreshortening (i.e., shortening of slopes facing the satellite in radar coordinates, see Figure 1) and shadowing (i.e., lack of information behind an obstructing object) present a clear drawback as they limit the precision and applicability of the technique in subregions of the images. Furthermore, while changes in amplitude are heavily driven by topography, changes in the backscattering properties of the ground such as soil moisture and roughness can modulate the intensities in a radar image and thus present an additional constraint on radioclinometric methods. This property has been leveraged in several studies (e.g., Howell et al., 2019; Shiroma et al., 2022; Yang et al., 2018) to detect ground property changes using radar images where the influence of topography has been removed from the amplitude images through radiometric

terrain corrections (RTC). Other approaches exploit different radar signal polarizations to identify changes in surface roughness due to, for example, tephra deposits (Saepuloh et al., 2015).

Despite the shortcomings of oblique imaging geometries and possible complications due to temporally varying backscattering properties, we believe that, when carefully constrained, radioclinometry can fill an important observational gap resolving meter-scale morphological changes in which no other sources for repeat DEMs exist. Thus, here we modify a radioclinometric method developed by Frankot and Chellappa (1990), who defined the amplitude image intensity as the reflectance of the surface, which is a function of the DEM gradient and the radar cross section. We use this technique to obtain a DEM gradient for each amplitude image. The integral of these gradients gives us an elevation map estimate. Comparison of subsequent elevation map estimates allows us to construct time series of topographic change, even for volcanic eruptions where the morphology changes rapidly. We verify our implementation by estimating elevation changes produced by a simulated collapse in the 2019 crater of Shishaldin Volcano. To validate our method, we compare elevation change estimates inferred from TerraSAR-X observations at Mount Cleveland during its 2011–2012 eruption to estimates of dome growth inferred by Wang et al. (2015) and volume estimates inferred from thermal data by Werner et al. (2017). We then apply this method to the 2019–2020 eruptive episode at Shishaldin Volcano (Figures 2a and 2b) from TerraSAR-X High-Resolution Spotlight (HS) (Werninghaus & Buckreuss, 2009) images (Figure 2c). This eruption created large, thus far unquantified topographic change reported by the Alaska Volcano Observatory (AVO). As no syn-eruptive DEMs are available, the high resolution SAR that was acquired from multiple look angles throughout the event presents an opportunity for us to resolve morphological change and analyze the processes driving that change.

## 2. Method

Frankot and Chellappa (1990) defined the brightness in a radar amplitude image as a function of reflectance  $R$ , which depends on the surface slope of the target and its illumination vector,  $\beta$ :  $I(r, y) = R(u_r, u_y, \beta)$ , where  $I$  represents the brightness in the amplitude image as a function of the azimuth  $y$  and range  $r$  radar coordinates. The topography of the target is captured by  $u(x, y)$ . Thus,  $u_r$  is the gradient of the topography with respect to range ( $u_r = \partial u / \partial r$ ) (Figure 1) and  $u_y$  is the gradient of the topography with respect to azimuth ( $u_y = \partial u / \partial y$ ).

Frankot and Chellappa (1990) assumed the reflectance function  $R$  can be expressed as:

$$I = R = \eta \sigma_0 (u_r, u_y, \beta) A_l (u_r, u_y) + \sigma_{bias}^2 \quad (1)$$

where the albedo constant  $\eta$  is an isotropic scatter constant and  $\sigma_0$  is the radar cross section. The area illuminated by the satellite is defined as  $A_l(u_r, u_y) = \Delta r \Delta y |u_r|$  where  $\Delta r \Delta y$  is the surface area covered by the pixel. Because we are using radar coordinates, our horizontal spatial units are square pixels. Thus, we can substitute  $\Delta r \Delta y = 1$ . While more complex models exist, we can consider the radar cross section  $\sigma^0$  as a variation of the incidence angle  $\alpha$ , such that  $\sigma_0 = \cos \alpha = u_r / \sqrt{u_r^2 + u_y^2 + 1}$  (first model in Clapp, 1946). If we just consider a variation in range  $\sigma_0 \propto u_r / |u_r|$  and apply the definition for  $A_l$ , then  $I \propto u_r$ . The assumption of proportionality holds if the target area is small enough for the radiometric properties to not change, simplifying Equation 1 to:

$$\frac{\partial u}{\partial r} = a I(r, y) + b \quad (2)$$

where  $a$  is a proportionality constant and  $b$  is an error term capturing  $\sigma_{bias}^2$  in Equation 1. This relationship is visualized in Figure 2c, which shows that the amplitude reflectivity  $I(r, y)$  is correlated with the terrain, or the gradient of the DEM. Thus, in situations where our assumptions hold (i.e., the backscatter properties of the ground are constant in the area of study and illumination depends heavily on the gradient with respect to range coordinates), the gradient with respect to radar range becomes a linear combination of the amplitude reflectance and associated noise due to thermal and antenna effects.

We determine the constants  $a$  and  $b$  by solving the optimization problem formulated in Equation 3, which minimizes the difference between the range derivative,  $\frac{\partial u_{DEM}}{\partial r}$ , of a known DEM and the radar amplitude inferred topographic gradient (Equation 2). The amplitude image intensities must be driven by the topographic features of the region (Figure 2c) and the DEM needs to have a compatible resolution. In our application we use the



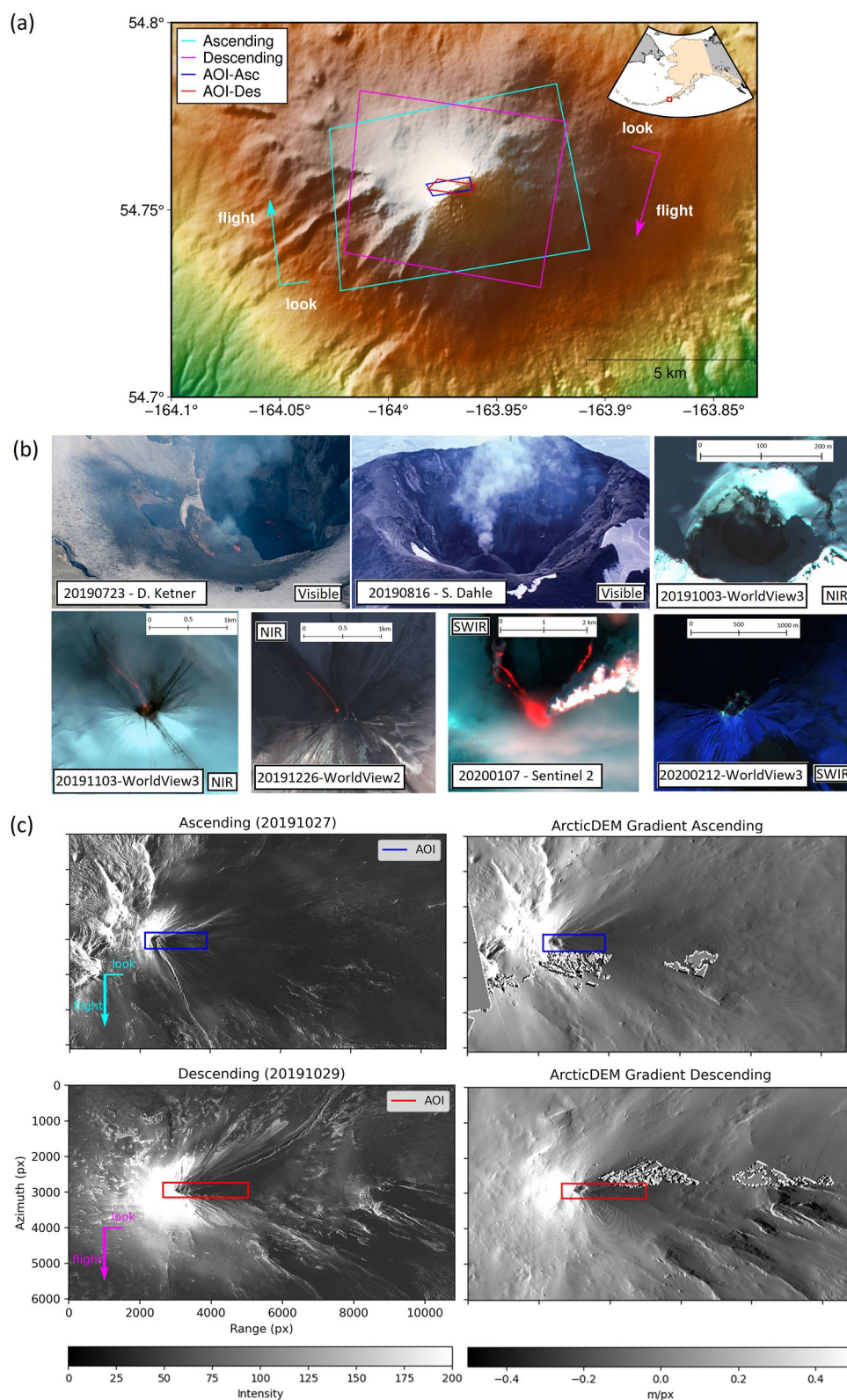


Figure 2.

ArcticDEM from August 2018 (Morin et al., 2016) projected into radar coordinates (Rosen et al., 2015). However, as ArcticDEM is based on photogrammetry techniques, cloud cover or severe shadow will result in coverage gaps. The optimization excludes pixels without DEM coverage.

$$F(a, b) = \frac{\partial u_{DEM}}{\partial r} - [aI(r, y) + b] \quad (3)$$

Once  $a$  and  $b$  are determined from a particular image, we can approximate the DEM from the amplitude image by integrating along the range coordinate. We can repeat the same process for any amplitude image where the spatial amplitude intensity variations are mostly related to topography. Thus, we introduce a subscript  $t$  to mark the time dependence of the DEM estimate,  $u_t$ , derived from the reflectivity,  $I_t$ , at time  $t$ :

$$u_t(y, r) = \int [aI_t(y, r) + b] \partial r + c \quad (4)$$

The integration term  $c$  is constant just along the range axis. However, along the azimuth axis it can change depending on the elevation of each azimuth coordinate. Thus, we have to solve a second optimization problem to find the optimal value for  $c$  for each azimuth line. In practical terms, this step aligns the amplitude-derived DEM to the true elevation profile, eliminating any undesirable artificial offsets. Thus, we can use the ArcticDEM as a constraint and write the cost function,  $H(c)$  which we intend to minimize for a particular azimuth coordinate  $y$ , as:

$$H(c) = u_{DEM}(r, y) - \int [aI_t(r, y) + b] \partial r + c \quad (5)$$

As we are operating in discretized image space, the integral becomes a sum along the range for each azimuth coordinate. Additionally, as the second optimization (Equation 5) is performed for each azimuth line, it makes sense to do the same for the first optimization problem (Equation 3). Hence, an amplitude pixel intensity  $I_t(r, y)$  in radar coordinates ( $y$  coordinate along azimuth,  $r$  coordinate along range) can provide an elevation  $u_t(r, y)$  in radar coordinates once we determine optimal values for the parameters  $a(y)$ ,  $b(y)$  and  $c(y)$  (Equation 6):

$$u_t(r, y) = \sum_{k=0}^r [a(y)I_t(k, y) + b(y)] + c(y) \quad (6)$$

This is a simplification of the method Frankot and Chellappa (1990) developed. Frankot and Chellappa (1990) expected variations in the radar cross sections along the range and azimuth axes, and they reconstruct elevations from inverse Fourier transforms. We assume that variations in the radar cross section only occur along the range axis as the illumination source is the same as the viewing source, and our elevation reconstruction is simpler. We also assume that possible discrepancies between satellite trajectories during each time step are corrected by the coregistration of both images (Rosen et al., 2015). Once we estimate a DEM from an individual amplitude image, we can repeat this step for any later amplitude image. Differencing the resultant DEMs from prior amplitude images will highlight terrain changes between acquisitions.

## 2.1. Inversion

We have two optimization problems that can be solved independently at each time step and we have introduced their cost functions (Equations 3 and 5). To determine the constants  $a$ ,  $b$ , and  $c$  for every azimuth coordinate  $y$  we can write both optimization problems in matrix form  $\mathbf{d} = \mathbf{G}\mathbf{m}$ . For Equation 3, the elements on  $\mathbf{d}$  are the pixels in the DEM gradient along range  $\frac{\partial u}{\partial r}$ , the entries for  $\mathbf{m}$  are the constants  $a_y$  and  $b_y$  for a particular azimuth  $y$ , and the

**Figure 2.** (a) Shishaldin Volcano map with inset showing its location in Alaska. TerraSAR-X ascending and descending coverage is shown by outlines. (b) Optical images showing growth and collapse of scoria cones during August, September, October and part of November and lava flows during November, December and January, WorldView-2 and 3 imagery are © 2019–2020 DigitalGlobe accessed via the NextView license. (c) Comparison of amplitude images for ascending and descending directions (in radar coordinates) with the gradients of the ArcticDEM (Morin et al., 2016) projected into the respective radar viewing geometry. The red and blue squares represent the Area of Interest (AOI) for each geometry. The artefacts are holes in the ArcticDEM due to clouds, fog, shadows, and other atmospheric obstructions. Note the similarity between radar intensity and topographic gradients.

matrix  $\mathbf{G}$  is the model consisting of a column of amplitude intensities and a column of ones. Thus, for a single azimuth coordinate  $y$  we can write (Equation 7):

$$\frac{\partial \mathbf{u}}{\partial r} = \mathbf{Gm} \quad (7)$$

$$\begin{bmatrix} \frac{\partial u_{y1}}{\partial r} \\ \frac{\partial u_{y2}}{\partial r} \\ \vdots \\ \frac{\partial u_{yn}}{\partial r} \end{bmatrix} = \begin{bmatrix} I_{y1} & 1 \\ I_{y2} & 1 \\ \vdots & \vdots \\ I_{yn} & 1 \end{bmatrix} \begin{bmatrix} a_y \\ b_y \end{bmatrix}$$

where  $\frac{\partial u_{yi}}{\partial r}$  is the  $y, i$  pixel in the DEM gradient, the  $I_{yi}$  is the  $y, i$  pixel in the amplitude image,  $a_y$  and  $b_y$  are the scaling constant and offset parameters for the azimuth  $y$ . For Equation 5, accordingly, the entries for  $\mathbf{d}$  are the difference between the DEM and the integration of the gradient derived from the amplitude image (Equation 2), while the sole entry for  $\mathbf{m}$  is constant  $c_y$  resulting in  $\mathbf{G}$  containing a column vector of ones. In matrix form for a single azimuth coordinate  $y$ , we can write (Equation 8):

$$\Delta \mathbf{u} = \mathbf{Gm} \quad (8)$$

$$\begin{bmatrix} u_{y1} - a_y I_{y1} - b_y \\ u_{y2} - a_y (I_{y1} + I_{y2}) - 2b_y \\ \vdots \\ u_{yn} - a_y \sum_{k=1}^n [I_{yk}] - nb_y \end{bmatrix} = \begin{bmatrix} 1 \\ 1 \\ \vdots \\ 1 \end{bmatrix} \begin{bmatrix} c_y \end{bmatrix}$$

where  $c_y$  is the integration constant for the azimuth  $y$ . To solve the first optimization problem (Equations 3 and 7), we need to compute the gradient from the ArcticDEM. However, we can forego this intermediate step, and source of potential additional error, by merging the two optimization problems (Equations 7 and 8) into one as formulated in Equation 6. In this case, the entries for  $\mathbf{d}$  correspond to the values in the ArcticDEM and the entries model vector  $\mathbf{m}$  are the constants for the azimuth  $y$ :  $a_y$ ,  $b_y$  and  $c_y$ . The matrix form for azimuth  $y$  then becomes (Equation 9):

$$\mathbf{u} = \mathbf{Gm} \quad (9)$$

$$\begin{bmatrix} u_{y1} \\ u_{y2} \\ \vdots \\ u_{yn} \end{bmatrix} = \begin{bmatrix} I_{y1} & 1 & 1 \\ I_{y1} + I_{y2} & 2 & 1 \\ \vdots & \vdots & \vdots \\ \sum_{k=1}^n I_{yk} & n & 1 \end{bmatrix} \begin{bmatrix} a_y \\ b_y \\ c_y \end{bmatrix}$$

Solving this equation for all azimuth coordinates  $y$  will yield the optimal  $a_y$ ,  $b_y$  and  $c_y$  constants for each azimuth and thus provide a solution to map radar intensity values to topography.

## 2.2. Radar Effects

Reconstructing a DEM from an amplitude image acquired for Shishaldin Volcano on 29 Oct 2019, provides an initial check to verify the implementation of our approach as it shows no substantial height changes across the images (Figure S1 c-d first row and Figure S2 in Supporting Information S1). However, we notice biases that can be explained by the aforementioned radar imaging effects: speckle, shadow, and foreshortening.

Speckle is due to the interference pattern generated by individual scatterers within one resolution cell. This produces random values in the amplitude image. If we are estimating terrain slope directly from the backscatter intensity, we need to take into consideration any effects that modulate this signal without being directly related to slope. These effects will be more discernible for areas closer to the satellite as we might be sensitive to the superposition of certain scatterers that do not have the same surface material properties (e.g., dielectric properties) as their surroundings. Therefore, we apply a non-local means filter where we apply a low pass filter to 5 by five pixel patches along the azimuth and range axes (Figure S3 in Supporting Information S1) to mediate biases related to speckle effects in individual pixels.

Shadowing can occur where we have an obstructing object between the oblique radar signal and the surface it tries to image. At volcanoes, for instance, shadows occur on the far side of vents away from the satellite or on the crater floor when the slopes are too steep. We identify shadowed regions through histogram-based thresholding of the amplitude values (Figure S4 in Supporting Information S1).

The biases from foreshortening are related to the topographic features of the surface. Because foreshortening occurs when the ground surface differs significantly from the satellite reference surface, it projects upward slopes closer to the satellite than identical downward slopes. When the upward slopes are too steep, we have a superposition in the images for different areas. The regions that would show layover depend on the viewing geometry of the satellite. Even if two images are on the same path, that does not mean the satellite trajectories were the same. Therefore, we could have regions that present layover in one image but not in the other if azimuth and look angles change drastically such that coregistration cannot fix the biases.

Our method to map radar intensity to topography described by Equation 9 can mitigate biases due to foreshortening and layover if the area of interest has the same spatial coverage for uphill and downhill sections. In such a case we have fewer observations that are affected by these radar effects (uphill) than pixels that are not (downhill) (Figure 2c). However, since we apply a least squares inversion we can mitigate the influence of pixels that are susceptible to layover by simply applying lower weights to pixels that we believe are not reliable. Thus, our inverse problem could become a modified version of Equation 9,

$$\begin{aligned} \mathbf{d}_w &= \mathbf{G}_w \mathbf{m} \\ \mathbf{W} \mathbf{d} &= \mathbf{W} \mathbf{G} \mathbf{m} \end{aligned} \quad (10)$$

where  $\mathbf{W}$  is a diagonal matrix containing the weights given to each pixel along a particular azimuth.

### 2.3. Verification: Synthetic Test

To test and verify the implementation of this method and its ability to retrieve rapidly occurring elevation changes from radar intensity observations, we create a synthetic data set for a hypothetical collapse within a crater (Figure 3). We use a descending TerraSAR-X amplitude image over Shishaldin Volcano from 29 October 2020, from which we estimate elevations as described above. To simulate a collapse feature, we add a 3D negative Gaussian function with a maximum subsidence of 10 m (Figure 3a). From this, we recreated an amplitude image that includes the synthetic collapse (Figure 3b), using the same  $a$ ,  $b$ , and  $c$  parameters derived in the initial DEM inference. At this point we have two amplitude images: the original 29 October 2020, observation and a clone of this that includes the simulated intensity values of the collapse feature. From this we can test our ability to infer elevation change with just two amplitude images. Running the synthetic amplitude image through our workflow and subtracting the inferred DEMs from one-another yielded the expected result of elevation changes only in the region of simulated collapse, as the amplitude images are otherwise the same. In the simulated collapse area we recovered the exact amount of subsidence that we simulated. However, this could be the consequence of creating an unrealistic observing geometry that in reality would include shadowing effects, we had to integrate this into the reconstructed amplitude image. Since we established an amplitude threshold to decide whether a pixel is shaded or not, we could select random 'shaded amplitudes' from the distribution of amplitude values below this threshold. To select pixels from the subsidence feature that require shading, we calculated the lowest elevation that this method can retrieve on each pixel if an obstructing object is between the signal and some target (Figure 3c). Then, for values that are less than the lowest elevation, we assigned random 'shaded amplitudes'. From this shaded amplitude image (Figure 3c) we recovered reasonable amplitude values, albeit smaller than the maximum simulated values because of the simulated shading. The overall shape remains similar to the simulated collapse,



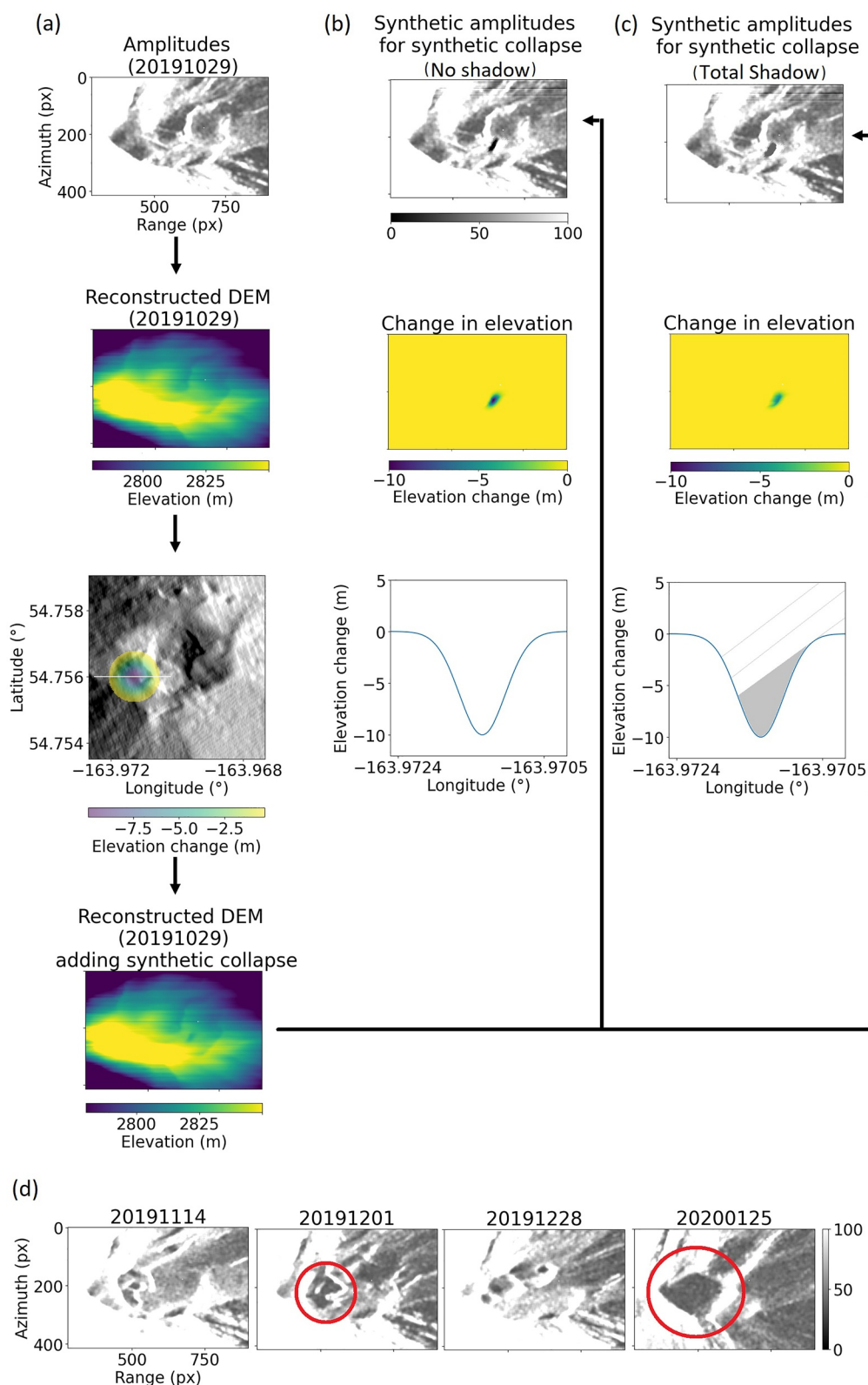


Figure 3.



which is representative of the trench that formed in the middle of Shishaldin Volcano's crater during the eruption (Figure 3d). Thus, we are confident that we can retrieve substantial surface change using this method, albeit not the full dynamic range if the viewing geometry is unfavorable.

According to this specific test, the hypothetical crater bottom was shadowed below 6 m of subsidence. Thus, the full 10 m of subsidence cannot be resolved by the method. This synthetic case demonstrates that in cases of shadowing, the percentage of resolved deformation (in our test Case 60%) naturally depends on how much of the resolved area remains visible to the satellite. The method, according to the synthetic case, has the same horizontal resolution as the amplitude image (1 m<sup>2</sup> in this case). The resolution does not change along the azimuth coordinates, but the range resolution changes with distance from the satellite. For pixels closer to the satellite (i.e., first coordinates in range) the resolution is about 2 m, but for pixels far in range the resolution increases to 0.66 m. For the synthetic case we use one image and modulate synthetic deformation onto a copy, thus ensuring that the radiometric properties between the images are identical. Therefore, the elevation change pattern is well defined. In the case of real observations, the vertical resolution will depend on how much the ground backscatter properties vary across a particular acquisition or region of interest. To estimate this uncertainty we can calculate the standard deviation of pixels that are within a known stable zone for each reconstructed DEM.

#### 2.4. Validation Case: 2011–2012 Mount Cleveland Dome Growth

Mount Cleveland (1,730 m), located at the western end of Chuginadak Island, is a symmetric, steep-sided volcano with a crater ~150 m wide and ~60 m deep. Its eruptions are generally Vulcanian and Strombolian and sometimes accompanied by lava flows, lava fountains and lava domes. In July 2011, lava extrusions began and a dome of 40 m height was detected in optical images. The dome dimensions remained almost constant during August after which it grew to a height of 80–85 m in September (McGimsey et al., 2014). Another period of no change in October was followed by subsidence and eventually explosive activity that destroyed the dome by the end of 2011. However, in January 2012 a new dome emerged (McGimsey et al., 2014). Wang et al. (2015) identified and tracked the boundaries of the dome in radar coordinates using Stripmap images from the TerraSAR-X mission. They derived height changes by using the incidence angle of the satellite signal. They found that the dome increased in height ~70 m between August and November 2011 and decreased in height in January 2012. Its area increased from 0.020 to 0.027 km<sup>2</sup> during October 2011. Werner et al. (2017) analyzed the same episode but used thermal data from the Moderate Resolution Imaging Spectroradiometer (MODIS) mission (Justice et al., 2002). They infer erupted lava volume from thermal energy radiated using an empirical relation (Coppola et al., 2013). This study relies on an empirical parameter called radiant density that depends on the rheological and topographic conditions for the studied lava body. Using different rheological compositions for the lava, Werner et al. (2017) estimated lava dome volume change between 0.5 and 1.4 Mm<sup>3</sup> between August and November 2011. These two independent results, one based on an entirely different data set, provide constraints against which we can validate our method.

We perform our inversions using the same data set from Wang et al. (2015) and the ArcticDEM from August 2018 (Morin et al., 2016). We estimated topographic change using the unweighted (Equation 9) and weighted (Equation 10) approaches. In the weighted approach, we assign less weight to the pixels that could have a high variance over time, and we explored different weight ratios to assess their influence on the results. In Figure 4a, we propose a way to construct the weight matrix, **W**, such that pixels that might present foreshortening and layover or where the topography can change drastically due to eruptive activity (teal zones in Figure 4) have less weight than pixels that we assume to be stable (purple zones in Figure 4). To compare our height change estimations with Wang et al. (2015) and Werner et al. (2017), we need to convert Werner et al. (2017) volume estimates to height changes first. We achieve this by deriving dome heights from the combination of volumes and dome area values Wang et al. (2015) estimated for the same period. Figures 5a–5c, 5e–5g show that in all cases our results correlate with both studies. However, the results from the unweighted solution are slight underestimated whereas the solution

**Figure 3.** Workflow for synthetic collapse test case: (a) Column shows the process to simulate a collapse inside Shishaldin Volcano crater. First, reconstruct digital elevation model (DEM) from the amplitude images, second simulate the collapse in geographical coordinates, third add the collapse to the reconstructed DEM, then simulate amplitudes and calculate changes of elevation for two different scenarios: (b) Without considering shadow and calculate change of elevation with such amplitude, and (c) Considering radar shadow effects and calculate change of elevation with such amplitude. (d) Real observation scenarios in Shishaldin Volcano crater that are similar to the synthetic case (red circles), compared to respective pre-collapse amplitude images on 2019-11-14 and 2019-12-28. Grayscales indicate intensity values in the amplitude images.

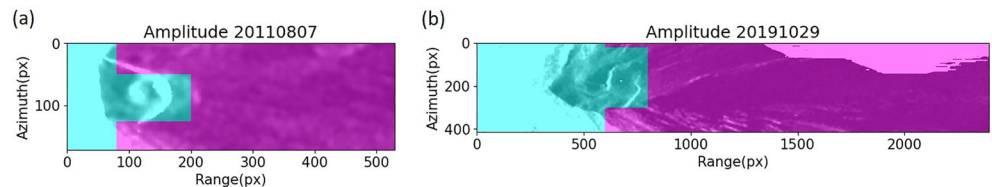


**Figure 4.** Amplitude image and assigning of weights for (a) Mount Cleveland and (b) Shishaldin Volcano. Teal zone represent the pixels with less weight, purple zone represent pixels with bigger weight.

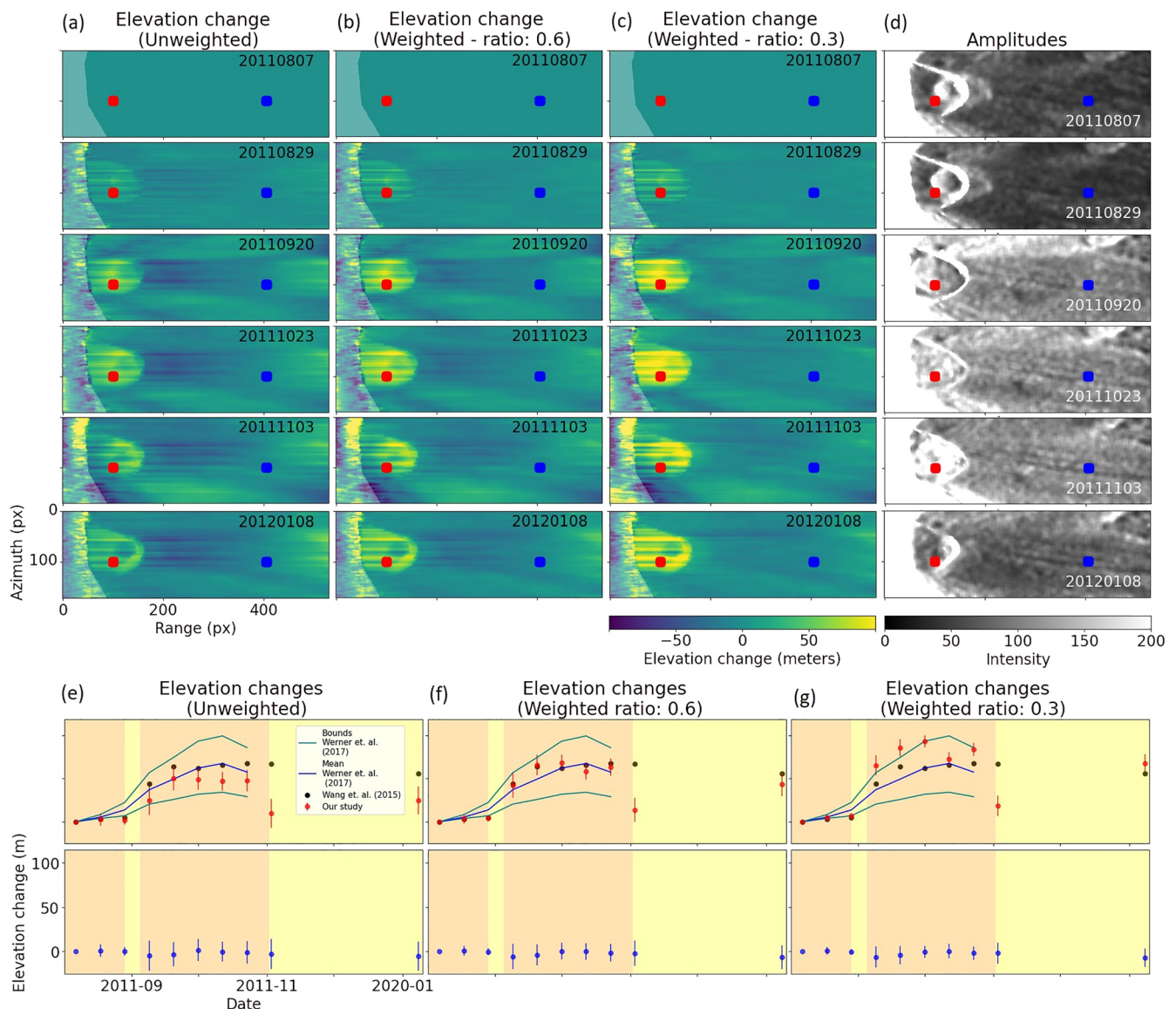


**Figure 5.** Elevation changes inferred from amplitude intensities in radar coordinates for Mount Cleveland using unweighted and weighted analyses, and compared to independent analyses. (a) Elevation change map using the unweighted approach. (b) Elevation change map weighting high-variance pixels at 0.6 of their original value. (c) Elevation change map using the weighted approach using a ratio of 0.3. (d) Corresponding amplitude images for each elevation change map. (e) Time series for red (in the crater) and blue (in area i.e., assumed to be stable) points in plot (a) using the unweighted approach. (f) Same as (e) but using the weighted approach with a ratio of 0.6. (g) Same as (e) but using the weighted approach with a ratio of 0.3. Light colored areas in (a), (b) and (c) represent a region with layover and foreshortening. Background colors in (e), (f) and (g) indicate the aviation color code for the 2011–2012 eruption.

that downweights the foreshortened and crater pixels to 0.3 of their value overestimates the results (Figure 5g). We reproduce the comparison studies best when using a weight of 0.6 (Figure 5f). An outlier on 3 November 2011, underestimates the Wang et al. (2015) results significantly. The SAR amplitude values are noticeably different between 2011 and 10-23 and 2011-11-03 (Figure 5d), perhaps reflecting some of the explosive activity resulting in the eventual destruction of the dome not resolved by Wang et al. (2015). Regardless, this exercise demonstrates that our method can calculate elevation changes using SAR amplitude images yielding similar results as independent analyses.

### 3. Case Study: The 2019–2020 Shishaldin Volcano Eruption

Shishaldin (Aleut: Sisquk or Sisagux) Volcano (2857 m), located near the center of Unimak Island at the tip of the Alaska Peninsula (Figure 2a), is a symmetric, steep-sided cone. According to the ArcticDEM, its crater has a diameter of ~200 m and it is ~40 m deep. Presently, snow falls on Unimak Island predominantly between October and May. With annual temperature variations between  $-5$  and  $12^{\circ}\text{C}$ , Shishaldin Volcano's edifice is mostly covered in perennial snow and ice (WRCC, 2016). Its composition is predominantly basaltic and the eruptions are generally Strombolian with ash and steam emissions, pyroclastic flows, lahars, and some persistent fumarolic activity in the summit crater (Neal & McGimsey, 1997; Stelling et al., 2002). Since 1775, 40 episodes of frequent small eruptions have been recorded (Stelling et al., 2002), making Shishaldin Volcano one of the most active volcanoes in the Aleutian Islands. Its most recent eruptive period began on 12 July 2019, indicated by increases in seismic activity, scoria cone growth and lava flows confined deeply in the summit crater. Seismicity and surface temperatures decreased during September 2019, but lava effusion and scoria cone growth restarted in mid-October 2019. During this period lava repeatedly overflowed the summit crater, resulting in lava flowing up to ~2 km down the northeastern and northwestern flanks. This melted snow and ice, creating lahars that reached the Bering Sea. Small collapse events produced minor ash fall and pyroclastic flows during this period. A large explosion on 12 Dec 2019 generated an ash plume rising to 7.5 km. This event triggered the collapse of the crater scoria cone, followed by a period of rebuilding of the cone and paroxysms of lava fountaining. The eruption continued through the beginning of January 2020 with cone growth and lava effusion, punctuated by collapses and ash emissions on January 3rd, seventh, and nineteenth. Ash clouds repeatedly reached altitudes up to 7.5 km. Activity progressively weakened until mid-March when cone growth and lava effusion within the summit crater briefly returned. Seismicity decreased and surface temperatures dropped along with a widening of the crater in the following months (AVO & Cameron, 2021). The 2019–2020 eruptive episode produced several rapid morphology changes of the summit crater due to spatter cone buildup and subsequent collapse. Optical sensors captured only a few clear views of the eruption (Figure 2b). TerraSAR-X acquired several high resolution observations of Shishaldin Volcano during this time of dynamic topography changes (Tables S1 and S2 in Supporting Information S1). We apply the method we developed above to this data set in an attempt to quantify these, thus far unresolved changes.

The topographic change we infer from TerraSAR-X backscatter amplitude observations between 29 October 2019, and 2 July 2020, using both weighted (consistent with the scheme in Figure 4b) and unweighted inversions is shown in Figure 6. This includes volume change estimates for regions inside the crater (green points in Figures 6d and 6e) when the standard deviation in the stable zone is less than 7 m. The time series error bars represent the standard deviation at pixels for which we do not expect significant elevation changes (i.e., after range coordinate 1,500, see Figure S5 in Supporting Information S1). These uncertainties are reduced in the weighted inversion, suggesting that this approach improves the resolution of smaller elevation changes. Our solutions highlight changes due to volcanic activity at Shishaldin Volcano during that period, which are broadly reflected by the aviation color code (this refers specifically to aviation risk; Guffanti and Miller (2013)). We see spatially extensive increases in elevation of up to 20 m between October 2019 and the end of December 2019 (Figures 6a and 6b and red and gray points in Figures 6d and 6e). This elevation increase is related to the growth of a scoria cone and lava flows spilling down the flanks spotted on optical images (Figure 2b). We can see this cone clearly emerge as a spatially coherent pattern inside of the crater in the elevation change map for 9 November 2019, in Figures 6a and 6b. We estimate a volume between 0.1 and 0.15  $\text{Mm}^3$  (depending on the approach) for this scoria cone. Additionally, we observe a step decrease in the elevation time series inside the crater (red point in Figure 6) after 7 January 2020 (Figures 6d and 6e, marked by red vertical line). On this date, a large explosion associated with the violent removal of material and the collapse of the vent region resulted in a change of the aviation



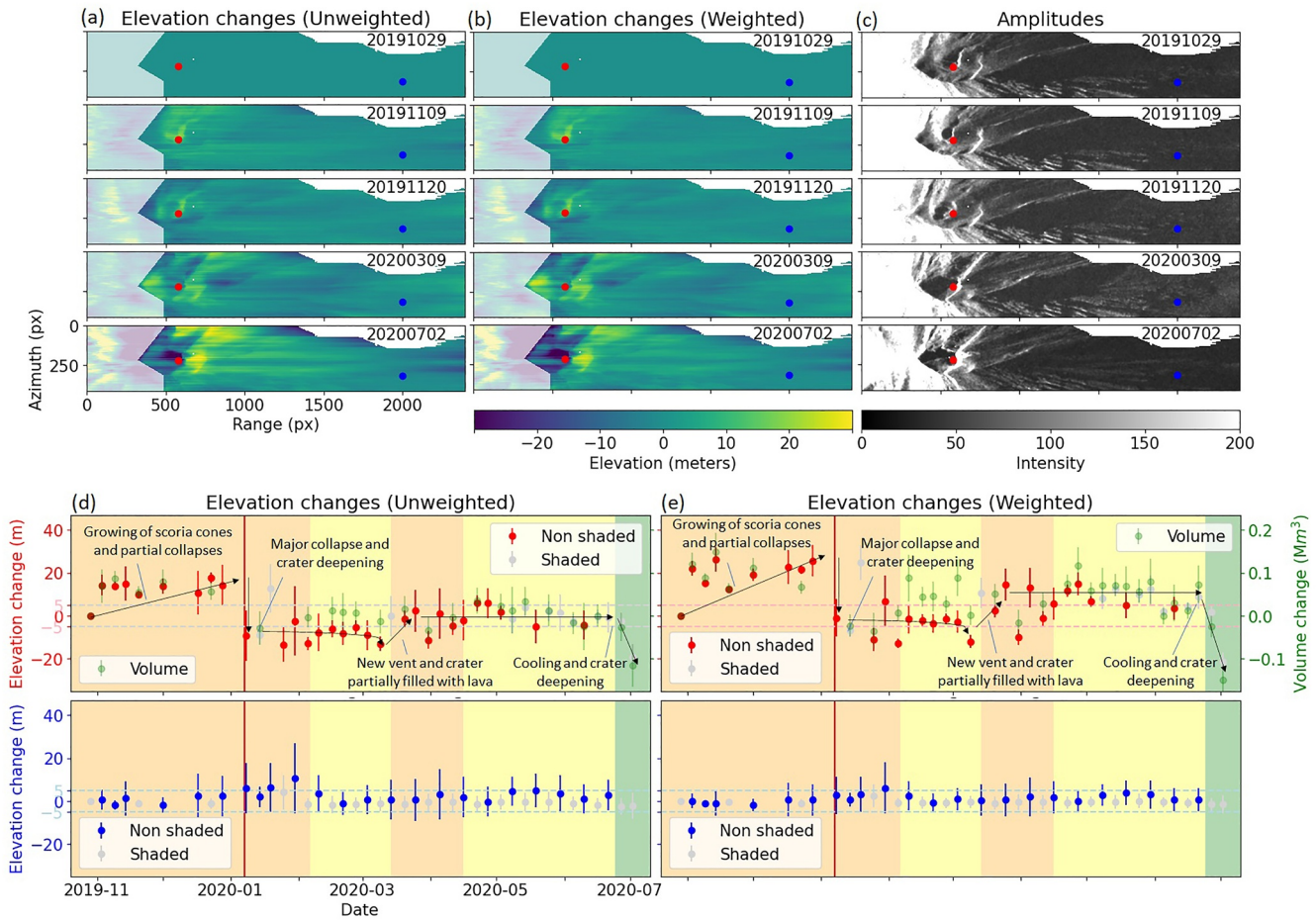


**Figure 6.** Shishaldin Volcano elevation change results for unweighted and weighted inversion in the descending direction in radar coordinates. (a) Elevation change maps inferred using an unweighted inversion, red and blue dots indicate locations for time series shown in (d). (b) Elevation change maps inferred by downweighting regions with expected foreshortening at a ratio of 0.6 in the inversion, red and blue dots indicate locations for time series shown in (e). (c) Corresponding amplitude images for each elevation change map. (d) Time series for red (in the crater) and blue (in area i.e., assumed to be stable) points in panel (a) background colors represent the aviation color code for the 2019–2020 eruption, gray points show an estimate for shaded pixels. (e) Time series for red and blue points in plot (b) otherwise similar to panel (d). Green points in (d) and (e) show volume estimates for the scoria cone growth and collapse.

color code/volcano alert level to Red/Warning. We estimate a similar volume for this change as the scoria cone, suggesting its complete destruction. Following this, we observe slight continued elevation decrease until March 2020 (Figure 6d), coinciding with reported deepening of the main crater that is best resolved by the weighted inversion (Figure 6e). The spatial extent of the collapse and deepening is resolved on the elevation change maps for 9 March 2020 (Figures 6a and 6b). The time series (Figures 6f and 6e) also resolves a subtle increase in elevation of ~5 m that could be related to renewed cone growth in mid-March 2020. However, these changes are almost indiscernible in the volume change estimates. From April until May 2020, we observe a predominantly stable period that coincides with a decrease in surface temperature and in seismic activity. Finally, decreases in elevation and volume after May 2020 agree with a widening of the crater. The weighted and unweighted analyses resolve elevation changes that agree with the volcanic activity. Comparison of the active crater results to the elevation changes over time within a presumably stable region outside of the active crater area (blue dots and time series in Figure 6) shows that the method infers only subtle elevation changes within the analysis uncertainty for the stable region (<5 m according to the variance for blue and gray points in Figures 6d and 6e). A visual interpretation (Figure 6c) of the amplitude images also suggests agreement with the inferred elevation changes. For instance, the change in brightness between October 29 and 9 November 2019, in Figure 6c can be interpreted as the growth of a cone, and our method indicates an increase in elevation in the same area when we look at the elevation change maps for 9 November 2019 (Figures 6a and 6b). Following this, the brightness remains almost constant from November 9–20, 2019, which is also reflected in the time series as the change in elevation between



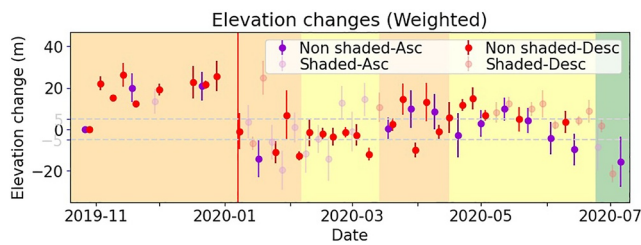


**Figure 7.** Elevation change time series for the red point inside the crater in Figure 6a in ascending and descending directions using the weighted inversion described in the text. The gray dashed lines indicate the average uncertainty of the method.

those dates remains within the uncertainty. Finally, we see a decrease in the brightness inside the crater on 9 March 2020, which does not change by 2 July 2020 (Figure 6c); this visually indicates a collapse that is quantified in the time series where we see a change in elevation greater than 20 m (after 31 December 2019, in Figures 6d and 6e).

The elevation change time series for the ascending direction shows a similar features, but with many more shaded observations in early 2020. Since the reference dates for ascending and descending directions are close (29 October 2019, for the descending path and 27 October 2019, for the ascending path), reducing the likelihood of introducing substantial biases during this ongoing eruption, we merge both time series into one (Figure 7). This denser time series clearly shows the same features we describe above: growing of the scoria cone until it gets destroyed in early January 2020. Following this major

collapse we observe a period of crater deepening and then renewed vent growth and partial filling of the crater with lava. Notably, the higher density of non-shaded ascending pixels toward the end of the time series amplifies the crater deepening we inferred from shaded descending observations, suggesting an earlier onset of this process.

Figures 8 and 9 show geocoded versions of the time series in Figures 6 and 7, for the weighted and unweighted inversions, respectively. We observe similar elevation changes in both orbit directions. The small estimated elevation changes in pixels far away from the crater where we expect no deformation emphasize the significance of

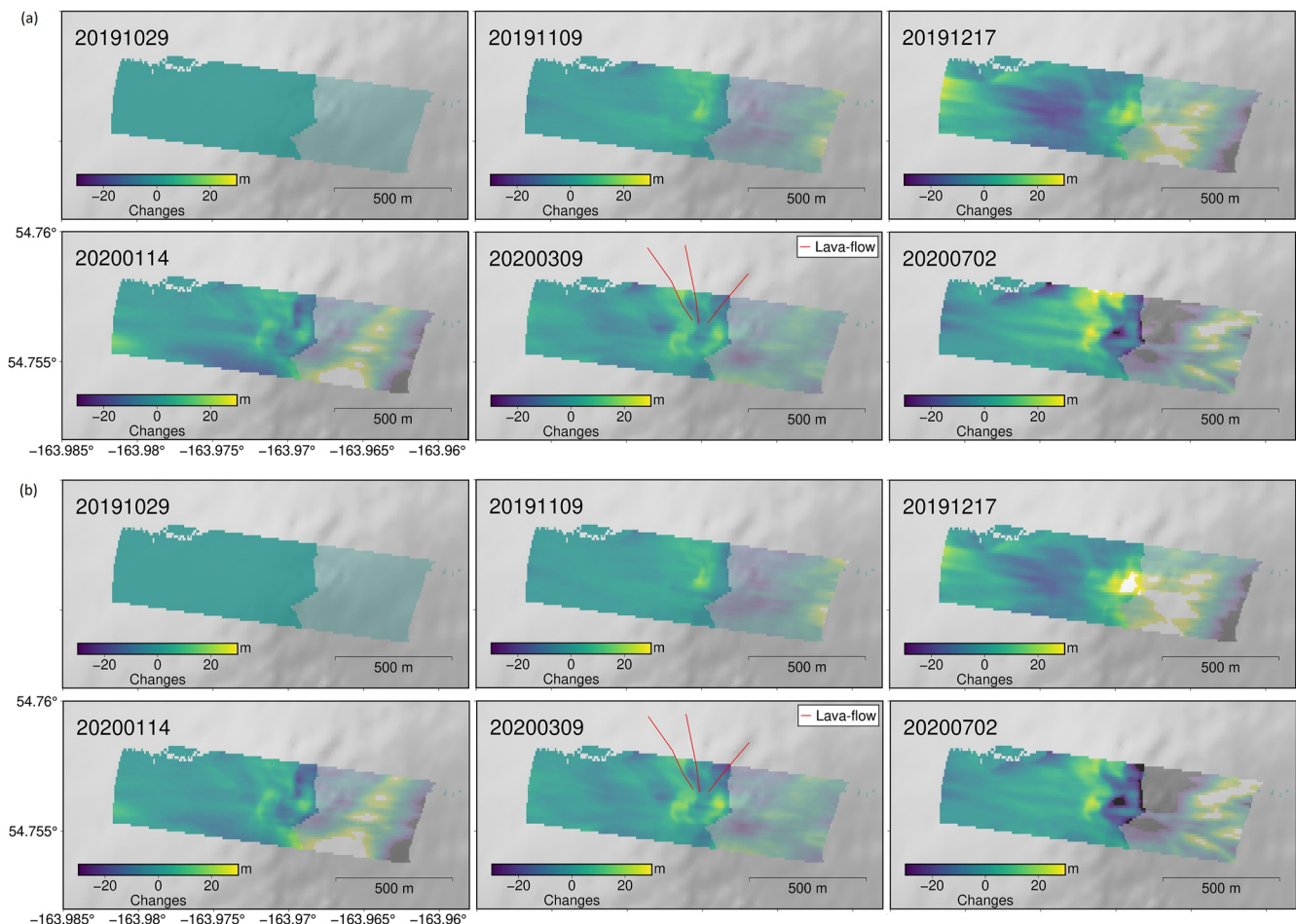


**Figure 8.** Geocoded cumulative elevation change maps for the descending direction relative to the first image in the sequence (20191029). (a) Results from unweighted inversion, red lines in the time step 20200309 represent the lava flow routes on Shishaldin Volcano at that time. (b) Results using weighted inversion, other conventions similar as (a).

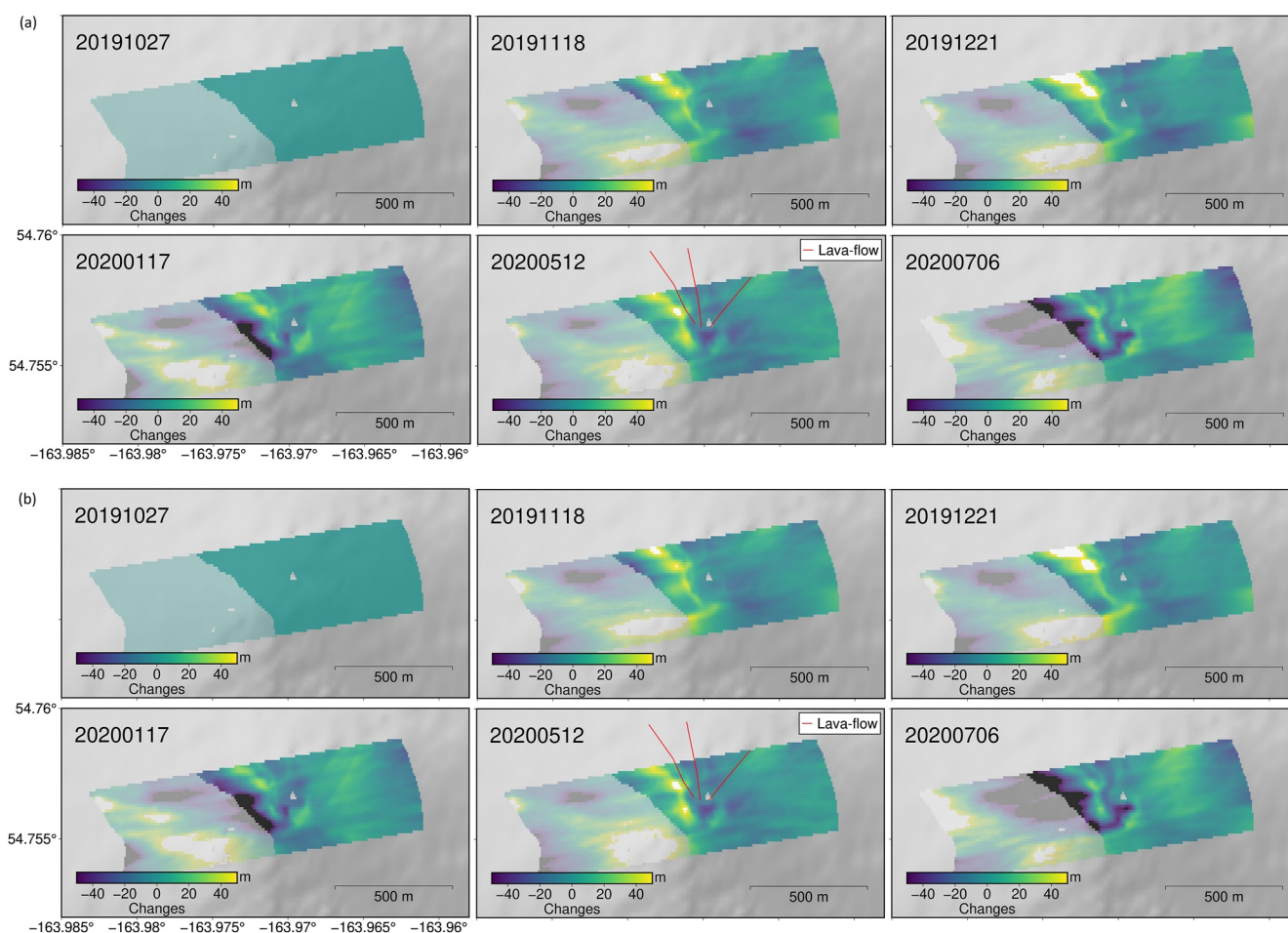


**Figure 9.** Geocoded cumulative elevation change maps for the ascending direction relative to the first image in the sequence (20191027). (a) Results using unweighted inversion, red lines in the time step 20200512 represent the lava flow routes on Shishaldin Volcano at that time. (b) Results using weighted inversion, other conventions similar as (a).

near crater elevation changes exceeding 20 m. However, the changes in the ascending direction are larger than the ones in the descending direction as different viewing geometries highlight different features. We see a similar pattern in the crater: crater filling until 7 January 2020, and then a major collapse. We also identify lava flows. According to optical satellite imagery (Figure 2b), lava flows followed three main paths, one in the northwest direction, one in the north direction and another in the northeast direction (Figure 2b). The northern and north-western paths are difficult to identify in our results as we approach the crater. We identify the trajectory for the north-northwestern path in the estimated elevation changes for the descending direction (time steps 20200309 and 20200702 in Figure 8), as well in the ascending direction (time steps 20200512 and 20200706 in Figure 9). This decrease in elevation is related to the melting of snow and ice, eventually generating lahars. The northeastern path is likely not captured by the inferred elevation change map, because the lava trench had already formed (see image from 3 October 2019, in Figures 2b and 2c), when the first amplitude image was acquired (27 October 2019). The paths estimated through elevation changes seem to match those observed in optical images from November and December, although they are only visible if the elevation changes produced are bigger than the uncertainty of our method (5 m) (Figure 2b).

#### 4. Discussion

We demonstrate that meter-scale topographic change is quantifiable from as few as two repeated SAR amplitude observations when the intensity is controlled mainly by the topographic variations as shown for the synthetic crater collapse case. This test verifies our implementation and shows that our method can estimate the magnitude

of topographic change even when the viewing geometry is unfavorable until radar shadowing prohibits the observation of the full extent of, for example, a collapsing region. The radar incidence angle is the predominant factor in the artifacts modulated onto a specific image: steeper views result in an increase of layover, while low-angle views increase shadows. Thus, some features might not be detected by one incidence angle, but appear when the incidence angle changes. For this reason, we classify the pixels as shaded (dark peak) and non-shaded via histogram-based thresholding of the amplitude values (Figure S4 in Supporting Information S1). This approach detects shaded pixels regardless of the viewing geometry. In addition to changes in viewing geometry, we also have to consider that the shape of evolving features is dynamic, which impacts which regions are shaded. Our Shishaldin Volcano case study illustrates in the images on 1 December 2019, and 25 January 2020 (Figure 3d), how a collapse feature can change in extent. Therefore, under constant incidence angle, a collapse that might be fully or partially shaded in one acquisition may be fully visible in a subsequent acquisition if its extent increases even if its depth remains constant. This introduces some uncertainty in the timing of the onset of observed topographic change. Features that are too small in their spatial extent (few pixels) might not be detectable at all. In our two applications, the image resolutions (1 m<sup>2</sup> for Shishaldin Volcano and 3 m<sup>2</sup> for Mount Cleveland), are high enough to detect changes in the volcanic craters as their areas (17,000 m<sup>2</sup> for Mount Cleveland crater and 31,000 m<sup>2</sup> for Shishaldin Volcano crater) contain multiple pixels that capture their morphology. The detection may be more difficult with lower resolution Sentinel 1 data, which may be useful for larger extent topographic change detection.

Our validation at Mount Cleveland shows that we are able to replicate substantial elevation changes previously inferred with different methods than the one developed here from MODIS (Werner et al., 2017) and TerraSAR-X data (Wang et al., 2015). The bounds inferred by Werner et al. (2017) give us a hint about the minimum ratio that we should use in our weighted approach (Figure 5). According to our results, a ratio less than 0.3 overestimates the elevation changes because information captured in foreshortened and layover pixels are substantially undervalued. To perform our weighted approach, we delimited broad zones informed by a qualitative assessment of the amplitude image as it may be impractical to precisely determine which pixels remain stable. However, there is no limit to the level of detail the weight matrix could contain. For instance, we could delimit just the foreshortening and layover zone, if we considered the majority of pixels within the crater stable. When all the pixels retain equal weight the elevation changes might be underestimated, but the method would still highlight regions of morphology changes. Compared to the Wang et al. (2015) solutions, we have to point out that we underestimate the results for 3 November 2011, in both weighted and unweighted approaches. However, volcanic activity reports describe subsidence and explosions between November 2011 and the beginning of 2012. Although it is not immediately clear whether we resolve this activity correctly, as this scene includes scatterers that have not been detected before that date, the amplitude image suggests substantial morphological changes in the crater, perhaps suggesting deflation or otherwise caused reorganization of the crater (Figures 5d, 3 November 2011). This agrees with the volcanic activity report that suggests the destruction of the dome during November and December and the growth of a new dome in January. Regardless, the remaining elevation changes we calculated fall well inside the confidence intervals from Werner et al. (2017) (Figures 5e–5g) and eight out of nine elevation changes from Wang et al. (2015) fall inside our own confidence intervals of the results from the inversion that used a 0.6 weighting ratio (Figure 5f).

Our analysis of data for the 2019–2020 Shishaldin Volcano eruption allows us to resolve and quantify several morphology changes that we cannot readily distinguish nor quantify with optical images due to weather conditions. The activity of the volcano as recorded by satellite and web camera imagery and reflected in AVO color code changes aligns with our observed morphology changes and the optical images that observed the crater, scoria cone, and lava flow activity. We find a general correlation between the volume estimates and the elevation changes. However, we observe some slight discrepancies during the time when the scoria cone is growing. For instance, before 7 January 2020, the volume change decreases slightly while the elevation changes slightly increase. Although the cone grew in height overall, the elevation change maps and overall volume change suggest zones of volume loss, which may represent lava overflowing the crater wall or occasional small partial cone collapses to the north, as well as growth and removal of material from the scoria cone summit crater (3 November 2019 and 20 November 2019 in Figures 6a and 6b). This highlights the sensitivity to small scale changes and their integration over small region when inferring derived products such as volume change.



The Shishaldin Volcano case study also shows the impact different viewing geometries have on our results. On one hand, different azimuth angles introduce different biases. For instance, in Figure 2c, we can see that regions with layover in the ascending images do not exhibit layover in the descending images. Similarly, in the ascending images, we would expect decreased resolution in the southwest part of the edifice and higher resolution in the northeast part of the edifice. This changes for the descending images, where the resolution on the northwest side of the edifice will be higher than on the southeast side. On the other hand, different incidence angles also have an influence in the results as discussed above. For instance, the time series for an area outside the crater (blue point in Figure 6) reveals a constant offset between consecutive dates (more noticeable in the unweighted inversion), which has correspondence with our two viewing geometries ( $42^\circ$  and  $51^\circ$  in Tables S1 and S2 in Supporting Information S1). However, when we look at the time series inside the crater, it is impossible to discern each group. In fact, the time series at the stable area indicates that the bias can be less than 3 m. This is a promising result as this opens the possibility to combine results from different satellite missions if the difference between their azimuth angles is negligible (less than  $2^\circ$ ) and their incidence angles do not change drastically (less than  $10^\circ$ ).

We have to consider other sources of noise in the elevation change maps. For instance, the seasonal changes at Shishaldin Volcano and Mount Cleveland can modulate the intensity in the amplitude images through changes in ground properties within our area of interest, and thus impact our topography change estimates (e.g., 16 August 2019, in Figure 2b). For Shishaldin Volcano, we have observations spanning October 2019 until July 2020. According to meteorological data, snow fall is expected between October and May. As we can see in the optical images, by the end of October Shishaldin Volcano's summit was covered in snow until June, which is expected as the temperatures do not change drastically on Unimak Island throughout the year (between  $-5$  and  $12^\circ\text{C}$ ). The time series for the crater and the stable area do not show systematic changes between April and June 2020 when we would expect to notice the changes in ground properties. In fact, this is the only time period during which we do not observe changes in the crater. Additionally, the optical image from 26 December 2019, shows the crater and nearby regions were not only covered by snow but also by tephra deposits. During the acquisition of the amplitude image on 3 November 2019, Shishaldin Volcano is predominantly covered in snow except for crater and lava flows. Therefore, we would expect systematic elevation changes due to changes in the radar reflectivity of the surface at those times. However, the elevation changes for those dates are similar (Figures 6d and 6e). This trend indicates that the influence of topography on the amplitude image intensity is bigger than changes in ground properties in steep terrains such as Shishaldin Volcano or Mount Cleveland (Figure S6 in Supporting Information S1). Nevertheless, RTC corrections could be employed to mediating the influence of ground property changes, but these corrections can potentially hide topographic features (Shiroma et al., 2022). The best option may be the use of different polarizations to discern topographic features from changes in roughness (Saepuloh et al., 2015). Although this is not always possible as many SAR sensors just gather one polarization.

With the method developed here, morphology changes can be observed at low latency, which is often of interest for ongoing eruptions. The most time consuming task is the coregistration of the images with the DEM ( $\sim 20$  min per pair), following which we have to select the area of interest and perform the inversions ( $\sim 5$  min per image). Our two applications to Mount Cleveland and Shishaldin Volcano demonstrate that the method can work with different resolutions and acquisition modes. However, the resolutions between stripmap ( $\sim 3\text{ m}^2$ ) and high-resolution spotlight ( $\sim 1\text{ m}^2$ ) modes are comparable. The method can potentially calculate elevation changes from different satellite acquisitions even if the products have different resolutions. However, the coregistration between different acquisitions might not be simple as InSAR software cannot be used (Rosen et al., 2015) in such a case. While the analysis of two acquisitions can capture the cumulative morphological change between them, to resolve the full dynamics of activity more than two consecutive acquisitions are required. For instance, were the acquisition times at Shishaldin Volcano separated by more than 1 year, the dynamics of the growth and subsequent collapse of scoria cones could not have been described.

Our method has some limitations and remaining issues. First, the elevation change maps depend on the reference image available. If the extension of the morphology changes is substantial in the remaining images with respect to the reference, the time series results could be poor as there may not be enough stable points available to constrain the inversions, especially the DEM alignment. Therefore, a good practice is the selection of a study area large enough to constrain every elevation map with stable zones that act as control points in the inversion, but small enough so the ground backscatter conditions remain largely constant. A second issue is the noticeable banding



between azimuth lines (e.g., Figures 6a and 6b). This is a consequence of the integration along the range axis and different biases that remain for each azimuth line even after the correction of radar effects, which then bias the full range integral. This issue can be addressed by selecting appropriate pixels using consistent amplitude values based on InSAR unwrapping techniques (Chen & Zebker, 2002). In this case, if the variance of a pixel is high between the acquisitions, we could discard it. However, choosing the appropriate variance threshold is not straightforward. Additionally, individual inversions for each azimuth coordinate can generate discontinuities in the reconstructed DEMs due to the changes in values for parameters  $a$ ,  $b$ , and  $c$  in Equation 6 between azimuth lines. We should note, however, that there is the possibility of doing just one inversion for all azimuths simultaneously using the appropriate design matrix and applying regularization to reduce the variations along the azimuth axis. Our attempts show that a single inversion can smooth the reconstructed DEMs slightly (Figure S7a in Supporting Information S1), but the calculation time increases exponentially due to the size of the design matrix. Since the discontinuities remain somewhat noticeable, and regularization enhances the variance between azimuth coordinates in the reconstructed DEMs (Figure S7 in Supporting Information S1), we did not choose this approach. This indicates that the integration along the range axis is the main source for the discontinuities in the final output. The discontinuities could be reduced if the inversion is performed in the frequency domain as is suggested by Frankot and Chellappa (1990), but this might affect the vertical resolution as changes in elevation could be masked when certain frequencies are discarded. Besides radar effect biases, the method is heavily dependent on the coregistration, and the resampling of the amplitude images can distort some pixels, leading to potential additional biases. If the overall amplitude changes drastically between the reference and the secondary images, the distortions in the secondary image will be significant.

## 5. Conclusions

We developed and validated a method to retrieve elevation changes from SAR amplitude intensity images from coregistered radar amplitude images and a DEM with a comparable resolution. The method consists of three main steps: first, an inversion to infer an elevation gradient from an amplitude image; second, integration of the resulting gradient and a second inversion to calculate the integration constants; and third, the mitigation of radar effects such as layover and shadow or possible changes in the backscatter properties of the ground on the inferred DEMs. Our approach merges the two first steps into a single inversion that maps amplitude values into elevation values. We expand this approach such that regions susceptible to layover or foreshortening can be downweighted in the inversion. With these, we are able to get a resolution of about 5 m for vertical changes in terrain through time. The horizontal spatial resolution depends on the SAR mission that is used (for TerraSAR-X HS mode image the resolution is on average 1 m<sup>2</sup>). The resolution on targets near to the satellite have less resolution than those far from it as expected for radar acquisitions. We have verified our implementation using a synthetic test case, validated the method against independent observations, and applied the method to quantify topographic change during the 2019–2020 Shishaldin Volcano eruption. Our verification case for a hypothetical collapse event shows that even when a collapse area is heavily influenced by shadowing, the method can retrieve elevation change until shadowing prevents the observation of this region. The validation step leveraged TerraSAR-X Stripmap images acquired during the 2011–2012 Mount Cleveland eruption. Our results are comparable to independent observations from Wang et al. (2015) using the same data but a different method to infer elevation change, and Werner et al. (2017) who determined eruption rates from MODIS thermal data. We applied the method to dozens of TerraSAR-X HS images that observed the 2019–2020 Shishaldin Volcano eruption. We create elevation change maps over time and resolve the topographic dynamics in time series for ascending, descending, and merged observations. Our results quantify the dynamic changes of cone growth, destruction, rebuilding and subsidence over the 8-month observation period. We estimate that the 2019–2020 summit scoria cone reached a total volume between 0.1 and 0.15 Mm<sup>3</sup> and a maximum height between 20 and 30 m prior to its complete destruction. Furthermore, we are able to resolve elevation decreases along documented lava flow paths where the melting of the substrate ice by the lava produces elevation loss. This method can help quantify meter-scale elevation changes due to rapid geological processes, such as the detection and quantification of morphology changes for volcanic eruptions with available SAR images.

## Data Availability Statement

Data are available via ESA after registration and approval (ESA, 2022). The Zenodo repository (<https://doi.org/10.5281/zenodo.6784982>) contains the codes and notebooks implementing the methods developed here (Angarita et al., 2022).

## Acknowledgments

We would like to thank Associate Editor Mike Poland, Rick Wessels, and the anonymous reviewers for their invaluable comments that improved our manuscript. MA was supported by NSF-EAR 1855126, RG was partially supported by NSF-EAR 2019232 and U.S. Geological Survey under Cooperative Agreement No. G21AC10384. Data are available via ESA after registration and approval. Any use of trade, firm, or product names is for descriptive purposes only and does not imply endorsement by the U.S. Government.

## References

- Angarita, M., Grapenthin, R., Plank, S., Meyer, F. J., & Dietterich, H. R. (2022). Quantifying crater morphology changes during the 2019–2020 Shishaldin Volcano eruption using SAR amplitude images. [dataset]. <https://doi.org/10.5281/zenodo.6784982>
- AVO, Alaska Volcano Observatory staff. (2021). In C. E., Cameron, (Ed.), *Shishaldin reported activity*. Retrieved from <https://www.avo.alaska.edu/volcanoes/activity.php?volname=Shishaldin%26page=basics%26eruptionid=4541>
- Chen, C. W., & Zebker, H. A. (2002). Phase unwrapping for large sar interferograms: Statistical segmentation and generalized network models. *IEEE Transactions on Geoscience and Remote Sensing*, 40(8), 1709–1719. <https://doi.org/10.1109/tgrs.2002.802453>
- Clapp, R. E. (1946). *A theoretical and experimental study of radar ground return*. Radiation Laboratory, Massachusetts Institute of Technology.
- Coppola, D., Laiolo, M., Piscopo, D., & Cigolini, C. (2013). Rheological control on the radiant density of active lava flows and domes. *Journal of Volcanology and Geothermal Research*, 249, 39–48. <https://doi.org/10.1016/j.jvolgeores.2012.09.005>
- Ebmeier, S., Biggs, J., Mather, T., Elliott, J., Wadge, G., & Amelung, F. (2012). Measuring large topographic change with InSAR: Lava thicknesses, extrusion rate and subsidence rate at Santiaguito Volcano, Guatemala. *Earth and Planetary Science Letters*, 335, 216–225. <https://doi.org/10.1016/j.epsl.2012.04.027>
- ESA, European Space Agency. (2022). TerraSAR-X archive [dataset]. ESA. Retrieved from <https://earth.esa.int/eogateway/catalog/terrasar-x-esa-archive>
- Frankot, R. T., & Chellappa, R. (1990). Estimation of surface topography from SAR imagery using shape from shading techniques. *Artificial Intelligence*, 43(3), 271–310. [https://doi.org/10.1016/0004-3702\(90\)90076-c](https://doi.org/10.1016/0004-3702(90)90076-c)
- Guffanti, M., & Miller, T. P. (2013). A volcanic activity alert-level system for aviation: Review of its development and application in Alaska. *Natural Hazards*, 69(3), 1519–1533. <https://doi.org/10.1007/s11069-013-0761-4>
- Horn, B. K. (1975). Obtaining shape from shading information. *The psychology of computer vision*, 115–155.
- Howell, S. E., Small, D., Rohner, C., Mahmud, M. S., Yackel, J. J., & Brady, M. (2019). Estimating melt onset over arctic sea ice from time series multi-sensor Sentinel-1 and Radarsat-2 backscatter. *Remote Sensing of Environment*, 229, 48–59. <https://doi.org/10.1016/j.rse.2019.04.031>
- Intrieri, E., Carlà, T., & Gigli, G. (2019). Forecasting the time of failure of landslides at slope-scale: A literature review. *Earth-Science Reviews*, 193, 333–349. <https://doi.org/10.1016/j.earscirev.2019.03.019>
- Justice, C., Townshend, J., Vermote, E., Masuoka, E., Wolfe, R., Saleous, N., et al. (2002). An overview of modis land data processing and product status. *Remote sensing of Environment*, 83(1–2), 3–15. [https://doi.org/10.1016/s0034-4257\(02\)00084-6](https://doi.org/10.1016/s0034-4257(02)00084-6)
- Kubaneck, J., Poland, M., & Biggs, J. (2021). Applications of biostatic radar to volcano topography—A review of 10 years of TanDEM-X. *Ieee Journal of Selected Topics in Applied Earth Observations and Remote Sensing*.
- Kubaneck, J., Richardson, J. A., Charbonnier, S. J., & Connor, L. J. (2015). Lava flow mapping and volume calculations for the 2012–2013 Tolbachik, Kamchatka, fissure eruption using bistatic TanDEM-X InSAR. *Bulletin of Volcanology*, 77(12), 1–13. <https://doi.org/10.1007/s00445-015-0989-9>
- Kubaneck, J., Westerhaus, M., Schenk, A., Aisyah, N., Brotopuspito, K. S., & Heck, B. (2015). Volumetric change quantification of the 2010 Merapi eruption using TanDEM-X InSAR. *Remote Sensing of Environment*, 164, 16–25. <https://doi.org/10.1016/j.rse.2015.02.027>
- Lombardi, N., Lorusso, R., Fasano, L., & Milillo, G. (2016). Interferometric COSMO-SkyMED spotlight DEM generation. In *2016 IEEE international geoscience and remote sensing symposium (IGARSS)* (pp. 6495–6498). <https://doi.org/10.1109/igarss.2016.7730697>
- Massonnet, D., Rossi, M., Carmona, C., Adragna, F., Peltzer, G., Feigl, K., & Rabaute, T. (1993). The displacement field of the landers earthquake mapped by radar interferometry. *Nature*, 364(6433), 138–142. <https://doi.org/10.1038/364138a0>
- McGimsey, R. G., Maharrey, J. Z., & Neal, C. (2014). *2011 volcanic activity in Alaska: Summary of events and response of the Alaska volcano observatory*. US Department of the Interior, US Geological Survey.
- Morin, P., Porter, C., Cloutier, M., Howat, I., Noh, M.-J., Willis, M., et al. (2016). ArcticDEM; a publicly available, high resolution elevation model of the Arctic. In *Egu general assembly conference abstracts* (pp. EPSC2016–8396).
- Neal, C., & McGimsey, R. G. (1997). *1996 volcanic activity in Alaska and Kamchatka: Summary of events and response of the Alaska volcano observatory*. US Department of the Interior, US Geological Survey.
- Pallister, J. S., Schneider, D. J., Griswold, J. P., Keeler, R. H., Burton, W. C., Noyles, C., et al. (2013). Merapi 2010 eruption—Chronology and extrusion rates monitored with satellite radar and used in eruption forecasting. *Journal of Volcanology and Geothermal Research*, 261, 144–152. <https://doi.org/10.1016/j.jvolgeores.2012.07.012>
- Poland, M. (2014). Time-averaged discharge rate of subaerial lava at Kilauea Volcano, Hawaii ‘i, measured from TanDEM-X interferometry: Implications for magma supply and storage during 2011–2013. *Journal of Geophysical Research: Solid Earth*, 119(7), 5464–5481. <https://doi.org/10.1002/2014jb011132>
- Poland, M., Hamburger, M., & Newman, A. (2006). The changing shapes of active volcanoes: History, evolution, and future challenges for volcano geodesy. *Journal of Volcanology and Geothermal Research*, 150(1–3), 1–13. <https://doi.org/10.1016/j.jvolgeores.2005.11.005>
- Pritchard, M. E., & Simons, M. (2002). A satellite geodetic survey of large-scale deformation of volcanic centres in the central Andes. *Nature*, 418(6894), 167–171. <https://doi.org/10.1038/nature00872>
- Rosen, P., Gurrola, E., Agram, P. S., Sacco, G. F., & Lavalley, M. (2015). The InSAR scientific computing environment (ISCE): A python framework for earth science. *Agui fall meeting abstracts, 2015*, IN11C–1789.
- Saepuloh, A., Koike, K., Urai, M., & Sumantyo, J. T. S. (2015). Identifying surface materials on an active volcano by deriving dielectric permittivity from polarimetric SAR data. *IEEE Geoscience and Remote Sensing Letters*, 12(8), 1620–1624. <https://doi.org/10.1109/lgrs.2015.2415871>
- Saito, M. (1969). Forecasting time of slope failure by tertiary creep. *Proc. 7th int. conf on soil mechanics and foundation engineering, mexico city*, 2, 677–683.
- Shiroma, G. H., Lavalley, M., & Buckley, S. M. (2022). An area-based projection algorithm for SAR radiometric terrain correction and geocoding. *IEEE Transactions on Geoscience and Remote Sensing*, 60, 1–23. <https://doi.org/10.1109/tgrs.2022.3147472>
- Stelling, P., Beget, J., Nye, C., Gardner, J., Devine, J., & George, R. (2002). Geology and petrology of ejecta from the 1999 eruption of Shishaldin Volcano, Alaska. *Bulletin of Volcanology*, 64(8), 548–561.

- Thomas, J., Kober, W., & Leberl, F. (1991). Multiple image SAR shape-from-shading. *Photogrammetric Engineering & Remote Sensing*, 57(1), 51–59.
- Toutin, T., & Gray, L. (2000). State-of-the-art of elevation extraction from satellite SAR data. *ISPRS Journal of Photogrammetry and Remote Sensing*, 55(1), 13–33. [https://doi.org/10.1016/S0924-2716\(99\)00039-8](https://doi.org/10.1016/S0924-2716(99)00039-8)
- Wang, T., Poland, M. P., & Lu, Z. (2015). Dome growth at Mount Cleveland, Aleutian arc, quantified by time series TerraSAR-X imagery. *Geophysical Research Letters*, 42(24), 10–614. <https://doi.org/10.1002/2015gl066784>
- Werner, C., Kern, C., Coppola, D., Lyons, J. J., Kelly, P. J., Wallace, K. L., et al. (2017). Magmatic degassing, lava dome extrusion, and explosions from Mount Cleveland volcano, Alaska, 2011–2015: Insight into the continuous nature of volcanic activity over multi-year timescales. *Journal of Volcanology and Geothermal Research*, 337, 98–110. <https://doi.org/10.1016/j.jvolgeores.2017.03.001>
- Werninghaus, R., & Buckreuss, S. (2009). The TerraSAR-X mission and system design. *IEEE Transactions on Geoscience and Remote Sensing*, 48(2), 606–614.
- Willey, R. L. (1984). Topography from single radar images. *Science*, 224(4645), 153–156. <https://doi.org/10.1126/science.224.4645.153>
- WRCC. (2016). *Western regional climate center*. National Oceanic and Atmospheric Administration. Retrieved from <https://wrcc.dri.edu/>
- Yang, Y., Wang, Y., Miao, X., & Li, H. (2018). Soil moisture retrieval with backscatter modeling and satellite datasets in Zoige wetland, China. In *IGARSS 2018-2018 IEEE international geoscience and remote sensing symposium* (pp. 9090–9093). <https://doi.org/10.1109/igarss.2018.8518748>
- Zebker, H. A., Werner, C. L., Rosen, P. A., & Hensley, S. (1994). Accuracy of topographic maps derived from ERS-1 interferometric radar. *IEEE Transactions on Geoscience and Remote Sensing*, 32(4), 823–836. <https://doi.org/10.1109/36.298010>
- Zhang, W., Zhu, W., Tian, X., Zhang, Q., Zhao, C., Niu, Y., & Wang, C. (2021). Improved DEM reconstruction method based on multibaseline InSAR. *IEEE Geoscience and Remote Sensing Letters*, 19, 1–5.
- Zink, M., Bachmann, M., Brautigam, B., Fritz, T., Hajnsek, I., Moreira, A., et al. (2014). TanDEM-X: The new global DEM takes shape. *IEEE Geoscience and Remote Sensing Magazine*, 2(2), 8–23. <https://doi.org/10.1109/mgrs.2014.2318895>